Low Phase Shift Filter for Current Sensing based on the Difference between AC Machine Models with and without Iron Losses

Niklas Himker, Marcel Krümpelmann and Axel Mertens
Leibniz University Hannover
Institute for Drive Systems and Power Electronics
Welfengarten 1
Hannover, Germany
Email: niklas.himker@ial.uni-hannover.de
URL: https://www.ial.uni-hannover.de

Acknowledgments

Keywords

≪AC machine≫, ≪Vector control≫, ≪Current sensor≫, ≪Field Programmable Gate Array≫

Abstract

For a current measurement with the goals of a high bandwidth and a high sampling rate, a filter with minimal phase shift is proposed. The filter is analytically derived using the differential equation of an induction machine (IM) model and is based on the difference in the stator current behaviour of machines with and without iron losses. To use this filter, only two parameters need to be set.

Introduction

To operate an electrical machine, current measurement and control are essential in most cases. Typically, the current for the control is measured once or twice per pulse-width-modulation (PWM) period of the converter. In a digital controller, analogue-to-digital (A/D) conversion is required, which can be performed by a sampling A/D converter [1, 2] or an averaging A/D converter [3]. Both systems introduce a phase shift of the measured quantity as a result of using the averaging filter, an analogue filter, or both of these.

In recent years, the use of the field programmable gate array (FPGA) in the field of self-sensing control has been investigated in order to implement oversampling of the A/D conversion with a sampling rate of $f_{AD} \geq 1\,\mathrm{MS/s}$ [4, 5]. By using oversampling, the bandwidth of the analogue filter is set higher than in a conventional design, introducing a lower phase shift. In this field of research, the effect of oversampling has not yet been investigated in an encoder-based field-oriented control (FOC).

Of course, the use of an FPGA with oversampling permits the implementation of a moving average filter, which leads to an averaging A/D converter. If only a few samples are used to implement the moving average filter, a lower phase shift is introduced. With regard to the high bandwidth of the analogue filter, this can lead to a measurement error, due to the influence of iron losses on the measured current. The iron losses introduce a superimposed step response of a first-order low-pass filter on the stator current of the electrical machine. For a converter-fed machine, this becomes apparent for each change in switching state. The time constant of the superimposed step response is mainly dependent on the leakage inductance and the iron loss resistance of the machine, leading to a small time constant (here:

$T_{\text{Fe}} < T_{\text{PWM}}$). This makes the measured current dependent on the time elapsed between the last switching instant of the converter and the sampling instant of the controller. In literature, iron losses have only been discussed with regard to the fundamental frequency-efficiency behaviour of an AC machine [6, 7].

The idea of this paper is to use the difference between machine models with and without iron losses as a current filter. The time constant T_{Fe} does not exist in the machine model without iron losses. The proposed filter estimates and subtracts the superimposed step response from the stator current of the machine. In this way, stator current measurement noise is reduced, as this is identified as a component of the superimposed step response of the iron losses. This can be beneficial for high dynamic current control as it reduces measurement noise and can increase the quality of state estimation for electrical machines. The proposed filter is analytically derived using the differential equation of the IM, and simplified to a grey box model with only two parameters, which can be easily tuned. The resulting transfer function of the filter with a small phase shift is discussed and it is validated in both simulations and an experimental investigation.
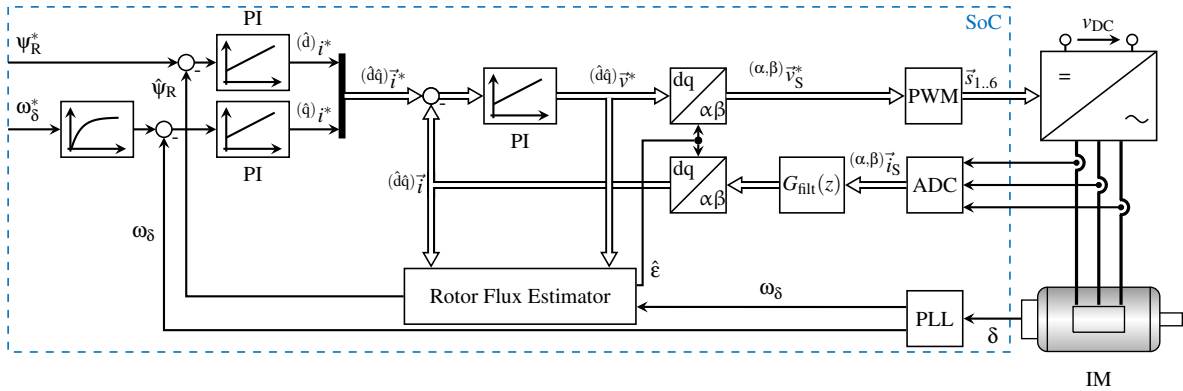
Fig. 1: FOC of the IM (feed-forward not shown)

Model of the Induction Machine

In this chapter, the models used to represent the IM are described. Initially, the fundamental model is presented, which is defined by the following differential equations in the (α, β) reference frame

$$^{(\alpha,\beta)}\vec{v}_{\text{S}} = R_{\text{S}}{}^{(\alpha,\beta)}\vec{i}_{\text{S,f}} + \frac{\text{d}}{\text{d}t}{}^{(\alpha,\beta)}\vec{\psi}_{\text{S,f}} \tag{1}$$

$$0 = R_{\text{R}}{}^{(\alpha,\beta)}\vec{i}_{\text{R,f}} + \frac{\text{d}}{\text{d}t}{}^{(\alpha,\beta)}\vec{\psi}_{\text{R,f}} - \mathbf{J}\omega_\delta{}^{(\alpha,\beta)}\vec{\psi}_{\text{R,f}} \text{ with } \mathbf{J} = \begin{pmatrix} 0 & -1 \\ 1 & 0 \end{pmatrix} \text{ and } \omega_\delta = \frac{\text{d}}{\text{d}t}\delta \ . \tag{2}$$

The stator voltage is $^{(\alpha,\beta)}\vec{v}_{\text{S}}$, R_{S} and R_{R} are the resistances, and $^{(\alpha,\beta)}\vec{i}_{\text{S,f}}$ and $^{(\alpha,\beta)}\vec{i}_{\text{R,f}}$ are the currents of the stator and rotor, respectively. The rotor angular position is δ. To transform from the rotor-oriented (x,y) reference frame to the stator-oriented (α, β) reference frame, the matrix

$$^{(\alpha,\beta)}\mathbf{T}_{(x,y)} = \begin{pmatrix} \cos(\delta) & \sin(\delta) \\ \text{-}\sin(\delta) & \cos(\delta) \end{pmatrix} \tag{3}$$

is used. The stator flux linkage $^{(\alpha,\beta)}\vec{\psi}_{\text{S,f}}$ and rotor flux linkage $^{(\alpha,\beta)}\vec{\psi}_{\text{R,f}}$ are defined by

$$^{(\alpha,\beta)}\vec{\psi}_{\text{S,f}} = L_{\text{S}}{}^{(\alpha,\beta)}\vec{i}_{\text{S,f}} + L_{\text{SR}}{}^{(\alpha,\beta)}\vec{i}_{\text{R,f}} \text{ with } L_{\text{S}} = L_{\text{SR}} + L_{\text{S}\sigma} \tag{4}$$

$$^{(\alpha,\beta)}\vec{\psi}_{\text{R,f}} = L_{\text{R}}{}^{(\alpha,\beta)}\vec{i}_{\text{R,f}} + L_{\text{SR}}{}^{(\alpha,\beta)}\vec{i}_{\text{S,f}} \text{ with } L_{\text{R}} = L_{\text{SR}} + L_{\text{R}\sigma} \ .$$

where L_{S} and L_{R} are the inductances and $L_{\text{S}\sigma}$ and $L_{\text{R}\sigma}$ are the leakage inductances of the stator and rotor, respectively. The magnetisation inductance is L_{SR}. The equivalent circuit of the fundamental IM

is shown in Fig. 2(a). Additionally, the magnetisation current

$$^{(\alpha,\beta)}\vec{i}_{\mathrm{M,f}} = {}^{(\alpha,\beta)}\vec{i}_{\mathrm{R,f}} + {}^{(\alpha,\beta)}\vec{i}_{\mathrm{S,f}} \tag{5}$$

is depicted. In the next step, the model of the IM with iron losses is introduced. In the equivalent circuit, the iron loss resistance R_{Fe} and iron loss current $^{(\alpha,\beta)}\vec{i}_{\mathrm{S,Fe}}$ are added in parallel to the magnetisation inductance, leading to the circuit of Fig. 2(b).


(a) Fundamental model

(b) Model with iron losses
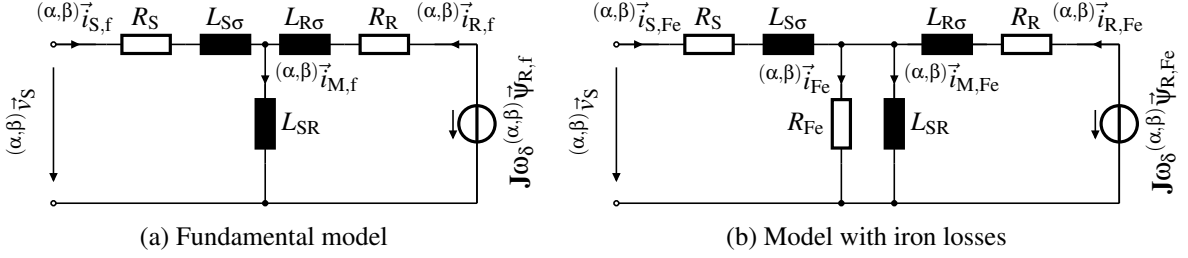
Fig. 2: Model of the IM used

The differential equation for the IM with iron losses is derived from its equivalent circuit [6] and results in

$$\frac{\mathrm{d}}{\mathrm{d}t}{}^{(\alpha,\beta)}\vec{i}_{\mathrm{S,Fe}} = \frac{1}{L_{\mathrm{S\sigma}}}\left[{}^{(\alpha,\beta)}\vec{v}_{\mathrm{S}} - (R_{\mathrm{S}} + R_{\mathrm{Fe}})^{(\alpha,\beta)}\vec{i}_{\mathrm{S,Fe}} - R_{\mathrm{Fe}}{}^{(\alpha,\beta)}\vec{i}_{\mathrm{R,Fe}} + R_{\mathrm{Fe}}{}^{(\alpha,\beta)}\vec{i}_{\mathrm{M,Fe}}\right] \tag{6}$$

$$\frac{\mathrm{d}}{\mathrm{d}t}{}^{(\alpha,\beta)}\vec{\psi}_{\mathrm{R,Fe}} = {}^{(\alpha,\beta)}\vec{\psi}_{\mathrm{M,Fe}}\left(-\frac{R_{\mathrm{Fe}}}{L_{\mathrm{SR}}L_{\mathrm{R\sigma}}} + \frac{R_{\mathrm{R}}}{L_{\mathrm{R\sigma}}} + \frac{R_{\mathrm{Fe}}}{L_{\mathrm{R\sigma}}} + \frac{R_{\mathrm{Fe}}}{L_{\mathrm{SR}}}\right) \tag{7}$$

$$+{}^{(\alpha,\beta)}\vec{\psi}_{\mathrm{R,Fe}}\left(\frac{R_{\mathrm{R}}}{L_{\mathrm{R\sigma}}} + \frac{R_{\mathrm{Fe}}}{L_{\mathrm{R\sigma}}}\right) + \mathbf{J}\omega_{\delta}{}^{(\alpha,\beta)}\vec{\psi}_{\mathrm{R,Fe}}$$

$$\frac{\mathrm{d}}{\mathrm{d}t}{}^{(\alpha,\beta)}\vec{\psi}_{\mathrm{M,Fe}} = R_{\mathrm{Fe}}{}^{(\alpha,\beta)}\vec{i}_{\mathrm{S,Fe}} + \frac{R_{\mathrm{Fe}}}{L_{\mathrm{R\sigma}}}{}^{(\alpha,\beta)}\vec{\psi}_{\mathrm{R,Fe}} - \frac{R_{\mathrm{Fe}}L_{\mathrm{R}}}{L_{\mathrm{SR}}L_{\mathrm{R\sigma}}}{}^{(\alpha,\beta)}\vec{\psi}_{\mathrm{M,Fe}} \quad . \tag{8}$$

The variables deviating from the fundamental-frequency model are marked with the subscript *Fe*. Additionally, the magnetisation flux linkage $^{(\alpha,\beta)}\vec{\psi}_{\mathrm{M,Fe}}$ is introduced. The flux linkages of the stator and rotor are defined by

$$^{(\alpha,\beta)}\vec{\psi}_{\mathrm{S,Fe}} = L_{\mathrm{S\sigma}}{}^{(\alpha,\beta)}\vec{i}_{\mathrm{S,Fe}} + {}^{(\alpha,\beta)}\vec{\psi}_{\mathrm{M,Fe}} \text{ and } {}^{(\alpha,\beta)}\vec{\psi}_{\mathrm{R,Fe}} = L_{\mathrm{R\sigma}}{}^{(\alpha,\beta)}\vec{i}_{\mathrm{R,Fe}} + {}^{(\alpha,\beta)}\vec{\psi}_{\mathrm{M,Fe}} \quad . \tag{9}$$

Deriving the Grey Box Model

The grey box model is derived in this section. The model is based on the equivalent circuit of an IM with iron losses. The effect of iron losses can be seen as a superimposed step response of a first-order low-pass filter on the stator current of the IM, if the machine is driven by a converter with a DC-voltage bus. This is shown in Fig. 5 by the current $^{(\alpha,\beta)}\vec{i}_{\mathrm{S,sim}}$. The idea of the grey box model is to filter the stator current in such a way that it does not contain the effect of the iron losses. In order to do this, the grey box model is derived in three steps:

1. Estimating the voltage $^{(\alpha,\beta)}\vec{v}_{\mathrm{M,Fe}}$ across the iron loss resistance R_{Fe}
2. Calculating the influence of the iron loss current $^{(\alpha,\beta)}\vec{i}_{\mathrm{Fe}}$ on the stator current $^{(\alpha,\beta)}\vec{i}_{\mathrm{S,Fe}}$
3. Subtracting the estimated current $^{(\alpha,\beta)}\vec{i}_{\mathrm{S,grey}}$ from the stator current $^{(\alpha,\beta)}\vec{i}_{\mathrm{S,Fe}}$

Estimating the Voltage Across the Iron Loss Resistance

The voltage $^{(\alpha,\beta)}\vec{v}_{\mathrm{M,Fe}}$ is defined by

$$^{(\alpha,\beta)}\vec{v}_{\mathrm{M,Fe}} = \frac{\mathrm{d}}{\mathrm{d}t}{}^{(\alpha,\beta)}\vec{\psi}_{\mathrm{M,Fe}} = R_{\mathrm{Fe}}{}^{(\alpha,\beta)}\vec{i}_{\mathrm{S,Fe}} + \frac{R_{\mathrm{Fe}}}{L_{\mathrm{R\sigma}}}{}^{(\alpha,\beta)}\vec{\psi}_{\mathrm{R,Fe}} - \frac{R_{\mathrm{Fe}}L_{\mathrm{R}}}{L_{\mathrm{SR}}L_{\mathrm{R\sigma}}}{}^{(\alpha,\beta)}\vec{\psi}_{\mathrm{M,Fe}} \quad . \tag{10}$$

By using the derivative of (10), the voltage can be described with the differential equation

$$\frac{L_{SR}L_{R\sigma}}{R_{Fe}L_R}\frac{d}{dt}{}^{(\alpha,\beta)}\vec{v}_{M,Fe} + {}^{(\alpha,\beta)}\vec{v}_{M,Fe} = \frac{L_{SR}L_{R\sigma}}{L_R}\frac{d}{dt}{}^{(\alpha,\beta)}\vec{i}_{S,Fe} + \frac{L_{SR}}{L_R}\frac{d}{dt}{}^{(\alpha,\beta)}\vec{\psi}_{R,Fe} \quad . \tag{11}$$

The goal of the derivation is to achieve an easy-to-implement filter. Equation (11) has two inputs ${}^{(\alpha,\beta)}\vec{i}_{S,Fe}$ and ${}^{(\alpha,\beta)}\vec{\psi}_{R,Fe}$. Both inputs are differentiated, which makes the voltage dependent on higher frequencies. The assumption is made that the derivative of the stator current is higher than the derivative of the rotor flux linkage, leading to $L_{R\sigma}\frac{d}{dt}{}^{(\alpha,\beta)}\vec{i}_{S,Fe} \gg \frac{d}{dt}{}^{(\alpha,\beta)}\vec{\psi}_{R,Fe}$. This is valid due to the derivative of the current ${}^{(\alpha,\beta)}\vec{i}_{S,Fe}$ being proportionally dependent on the voltage ${}^{(\alpha,\beta)}\vec{v}_S$, which is driven by the PWM and thus contributes the largest component at the switching frequency f_{sw} of the model. Making the assumption of $\frac{d}{dt}{}^{(\alpha,\beta)}\vec{\psi}_{R,Fe} \approx 0$, the equation is simplified to

$$\frac{L_{SR}L_{R\sigma}}{R_{Fe}L_R}\frac{d}{dt}{}^{(\alpha,\beta)}\vec{v}_{M,Fe} + {}^{(\alpha,\beta)}\vec{v}_{M,Fe} = \frac{L_{SR}L_{R\sigma}}{L_R}\frac{d}{dt}{}^{(\alpha,\beta)}\vec{i}_{S,Fe} \quad . \tag{12}$$

By simply using ${}^{(\alpha,\beta)}\vec{v}_{M,Fe} = {}^{(\alpha,\beta)}\vec{i}_{Fe}R_{Fe}$, the iron loss current can be estimated with

$$\frac{L_{SR}L_{R\sigma}}{R_{Fe}L_R}\frac{d}{dt}{}^{(\alpha,\beta)}\vec{i}_{Fe} + {}^{(\alpha,\beta)}\vec{i}_{Fe} = \frac{L_{SR}L_{R\sigma}}{R_{Fe}L_R}\frac{d}{dt}{}^{(\alpha,\beta)}\vec{i}_{S,Fe} \quad . \tag{13}$$

Calculating the Influence of the Iron Loss Current on the Stator Current

Using (13), the iron loss current ${}^{(\alpha,\beta)}\vec{i}_{Fe}$ can be calculated applying a first-order, low-pass filter to the measured stator current. This current is divided between the stator, rotor and magnetising paths. Its influence on the stator current can be written in the frequency domain as

$${}^{(\alpha,\beta)}\vec{i}_{S,grey} = {}^{(\alpha,\beta)}\vec{i}_{Fe}\frac{1}{j\omega L_{S\sigma}+R_S}\left(\frac{1}{j\omega L_{S\sigma}+R_S}+\frac{1}{j\omega L_{SR}}+\frac{1}{j\omega L_{R\sigma}+R_R}\right)^{-1} \quad . \tag{14}$$

The goal is to find the higher frequency component of this current, and then subtract it from the measured stator current. This makes the assumptions $j\omega L_{S\sigma} \gg R_S$ and $j\omega L_{R\sigma} \gg R_R$ reasonable, leading to $R_S = R_R \approx 0$ and resulting in

$${}^{(\alpha,\beta)}\vec{i}_{S,grey} = {}^{(\alpha,\beta)}\vec{i}_{Fe}\frac{1}{L_{S\sigma}}\left(\frac{1}{L_{S\sigma}}+\frac{1}{L_{SR}}+\frac{1}{L_{R\sigma}}\right)^{-1} \quad . \tag{15}$$

Subtracting the Estimated Current from the Stator Current

In the last step, the estimated current ${}^{(\alpha,\beta)}\vec{i}_{S,grey}$ is subtracted from the stator current ${}^{(\alpha,\beta)}\vec{i}_{S,Fe}$ to yield the estimated stator current without iron losses

$${}^{(\alpha,\beta)}\vec{i}_{S,filt} = {}^{(\alpha,\beta)}\vec{i}_{S,Fe} - {}^{(\alpha,\beta)}\vec{i}_{S,grey} \tag{16}$$

Combining all three steps leads to the block diagram in Fig. 3, with $K_1 = \frac{L_{SR}L_{R\sigma}}{L_R}$, $K_2 = \frac{1}{R_{Fe}}$, $K_3 = \frac{1}{L_{S\sigma}}\left(\frac{1}{L_{S\sigma}}+\frac{1}{L_{SR}}+\frac{1}{L_{R\sigma}}\right)^{-1}$ and $T_2 = \frac{L_{SR}L_{R\sigma}}{L_R R_{Fe}}$. In this block diagram, a rate limiter with a maximal slope of $2v_{DC}/L_{S\sigma}f_{AD}$ is added, in order to filter out any ringing effects from the current measurements.

The transfer function of the filter is given by

$$G_{grey}(s) = \frac{{}^{(\alpha,\beta)}\widehat{I}_{S,grey}(s)}{{}^{(\alpha,\beta)}\widehat{I}_{S,Fe}(s)} = \frac{sT_1}{1+sT_2} \quad \text{and} \quad G_{filt}(s) = \frac{{}^{(\alpha,\beta)}\widehat{I}_{S,filt}(s)}{{}^{(\alpha,\beta)}\widehat{I}_{S,Fe}(s)} = \frac{1+s(T_2-T_1)}{1+sT_2} \quad , \tag{17}$$
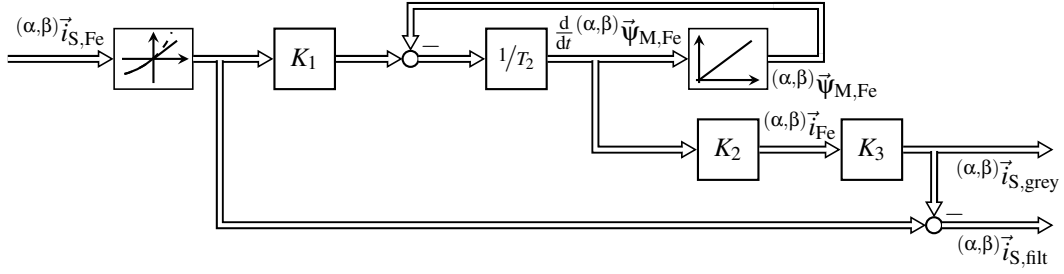
Fig. 3: Resulting filter of the IM to eliminate the superimposed step response

using $T_1 = K_1 K_2 K_3 = \frac{L_{SR} L_{R\sigma}}{L_R L_{S\sigma} R_{Fe}} \left(\frac{1}{L_{S\sigma}} + \frac{1}{L_{SR}} + \frac{1}{L_{R\sigma}} \right)^{-1}$. To determine the parameters of the grey box model, a time constant and a proportional gain (T_2 and T_1) need to be determined. In the transfer function of the filter, two time constants (T_2 and $T_2 - T_1$) must be tuned. Thus, only two parameters have to be analytically or empirically set, which makes this filter easy to implement even if the parameters of the machine are not known. The Bode plot of the filter is shown in Fig. 4. On the left-hand side, the plot for estimating $^{(\alpha,\beta)}\vec{i}_{S,\text{grey}}$ is depicted, and on the right-hand side, the Bode plot for $^{(\alpha,\beta)}\vec{i}_{S,\text{filt}}$ is shown.
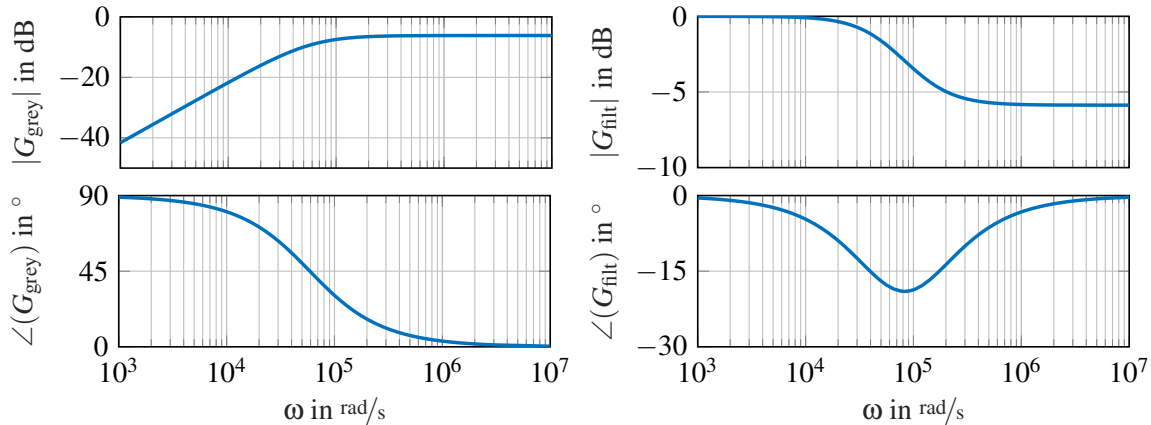
Fig. 4: Bode plot of the grey box model and the resulting filter

Discussion of the Characteristics of the Filter

The transfer function of the filter $G_{\text{filt}}(s)$ represents a general first-order transfer function with $T_2 > (T_2 - T_1) > 0$, leading to $G_{\text{filt}}(s \to \infty) < 1$. Thus, a low-pass filter with a minimal phase shift is introduced, which derives the IM current that would flow without iron losses from the measured current including iron losses. This can be used in a highly dynamic current control to reduce measurement noise. Another application can be found in the field of state estimation (e.g., rotor position) of machines. The filter can be used to improve the quality of the estimated parameters, as the measured current is less distorted by the high-frequency behaviour of the machine and the noise from the current sensor.

Simulation results using an FOC [8] of the IM and the filter are presented in Fig. 5. The control scheme used is shown in Fig. 1. In this paper, a switching frequency f_{sw} of $4\,\text{kHz}$ and a current measurement sampling rate f_{AD} of $1\,\text{MS/s}$ are used. In the simulation results, two cases are presented. In Fig. 5(a), an operating point with no load and high speed is shown. An operating point with rated torque and zero speed is shown in Fig. 5(b). On both graphs, the (d)-axis of the controller aligns with the (α)-axis of the machine. When comparing the currents at the two operating points, one can observe the superimposed step response of the first-order, low-pass component in the current $^{(\alpha,\beta)}\vec{i}_{S,\text{sim}}$. The filtered current $^{(\alpha,\beta)}\vec{i}_{S,\text{filt}}$ shows a constant slope during each switching state of the converter, meaning that it is independent of the iron loss current $^{(\alpha,\beta)}\vec{i}_{Fe}$.

(a) $n = 1000\,^{1}/\text{min}$ and $M = 2\,\text{Nm}$ (b) $n = 0\,^{1}/\text{min}$ and $M = 47\,\text{Nm}$
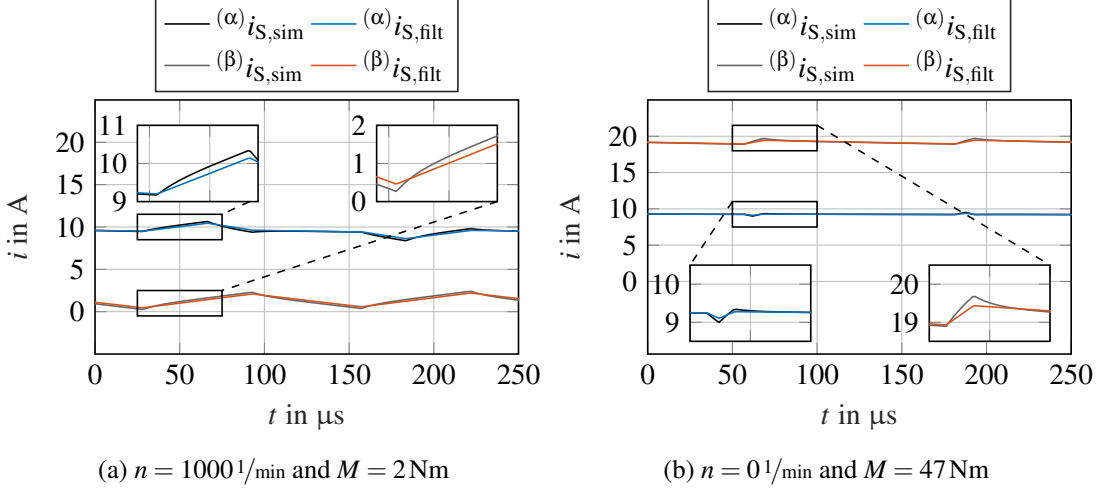
Fig. 5: Simulation results of the proposed filter

Experimental Results

To validate the simulation results, the filter is implemented on a test bench with an FPGA-based control system. The data concerning the used machine are given in Table I and a picture of the test bench is shown in Fig. 6. In order to validate the filter presented, two different current measurements are used. One measurement is based on a relatively low bandwidth Hall-effect current sensor ($f_{\text{BW},1} = 100\,\text{kHz}$) and the other measurement uses a shunt sensor with a higher bandwidth of $f_{\text{BW},2} = 300\,\text{kHz}$.

Table I: Machine data of the IM

Rated phase voltage (RMS)	V_{r}	230 V
Rated phase current (RMS)	I_{r}	15.2 A
Rated power	P_{r}	7.5 kW
Rated rotational speed	n_{r}	1,480 min^{-1}
Stator resistance	R_{S}	0.52 Ω
Rotor resistance	R_{R}	0.51 Ω
Iron loss resistance	R_{Fe}	250 Ω
Magnetisation inductance	L_{SR}	100 mH
Stator leakage inductance	$L_{\text{S}\sigma}$	3.5 mH
Rotor leakage inductance	$L_{\text{R}\sigma}$	3.4 mH
Number of pole pairs	p	2
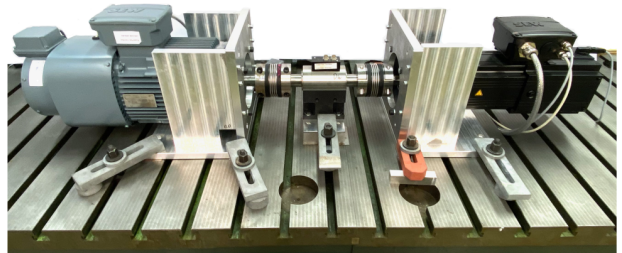
Fig. 6: Experimental test bench

Setting of Grey Box Model Parameters

Within simulations, the parameters of the filter are set by using the parameters of the IM. These parameters vary across the operating range of the IM, making the setting via analytical equation difficult. For the experimental validation, the parameters T_1 and T_2 are identified offline by parameter optimisation. The proposed method is presented, using the results of the shunt sensor. To determine the parameters, measurements of the machine are taken across the operating range. In this case, the setpoints of the rotor flux ψ_{R}^{*} and the current $^{(\hat{q})}i^{*}$ are varied throughout ranges of $\psi_{\text{R}}^{*} = [0.1, 0.15...1]\,\text{Vs}$ and $^{(\hat{q})}i^{*}[0, 2...20]\,\text{A}$. To achieve long switching states of the converter, a square-wave signal with an amplitude of $100\,\text{V}$ is used [9].

For each resulting operating point, the parameters of the filter are optimised in a two-step method. The first step is shown in the upper plot of Fig. 7(a). The current $^{(\alpha)}i_{\text{S,f,ref}}$ is fitted to the current $^{(\alpha)}i_{\text{S,shunt}}$ while the converter is in the passive switching state marked with ①. This is achieved using the model of the IM based on the fundamental behaviour ((1) and (2)). As inputs for the model, the actual switching state of the converter, the DC-link voltage, the current of the machine and the estimated flux are used.

Now the sum of leakage inductance of the stator $L_{S\sigma}$ and the rotor $L_{R\sigma}$ is varied until the sum of the square of the error of the first step $e_1 = {}^{(\alpha)}i_{S,f,ref} - {}^{(\alpha)}i_{S,shunt}$ is minimised. In the next step, the parameters T_1 and T_2 are optimised. The result of this optimisation is shown in the bottom plot of Fig. 7(a), marked with ②. In this case, each current sample is used to reduce the error of the second step $e_2 = {}^{(\alpha)}i_{S,filt,fit} - {}^{(\alpha)}i_{S,f,ref}$.

(a) Two-step method used for the parameter optimsation

(b) Results of the parameter optimisation
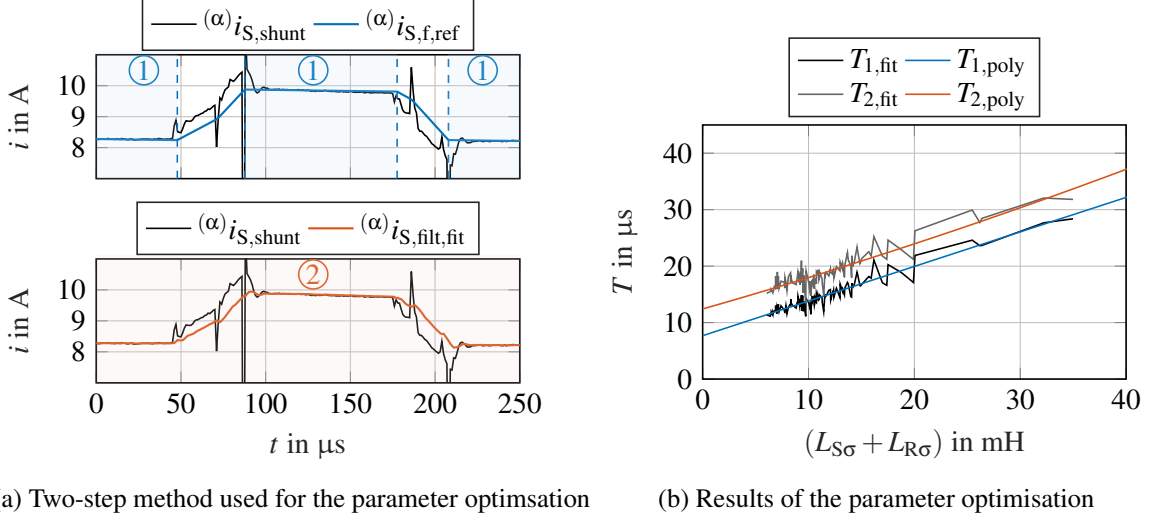
Fig. 7: Parameter optimisation of the proposed filter

The result of the parameter optimisation is shown in Fig. 7(b). Here, the parameters $T_{1,fit}$ and $T_{2,fit}$ are plotted against the sum of the leakage inductances $(L_{S\sigma} + L_{R\sigma})$. One can see that the results for this machine can be approximated with a first-order polynomial function of $T_{1,poly}$ and $T_{2,poly}$ and that the difference between the parameters $T_{1,poly}$, and $T_{2,poly}$ is approximately constant.

The results of the polynomial function are stored in a look-up table of the FPGA and are adapted online, using the sum of the leakage inductances $(L_{S\sigma} + L_{R\sigma})$ as an input. The sum of the leakage inductances $(L_{S\sigma} + L_{R\sigma})$ is estimated using the operating point of the machine described by the setpoints of the rotor flux ψ_R^* and the current ${}^{(\hat{q})}i^*$. For each operating point, the identified sum of the leakage inductances $(L_{S\sigma} + L_{R\sigma})$ is also stored in a look-up table of the FPGA. The same method is applied to the measurement using the Hall-effect current sensor.

Closed-Loop Performance of the Filter

The experimental results for no load at a speed of $n = 1000\,{}^1/\text{min}$ are shown in Fig. 8. The (d)-axis aligns with the (α)-axis of the machine. In each case, the offline optimised parameters $T_{1,poly}$ and $T_{2,poly}$ are used.

The results show reduced noise in the filtered current ${}^{(\alpha,\beta)}\vec{i}_{S,filt}$ for both sensors. In both measured currents ${}^{(\alpha,\beta)}\vec{i}_{S,Hall}$ and ${}^{(\alpha,\beta)}\vec{i}_{S,shunt}$, ringing appears at the switching instant of the converter leading to one or more distorted samples. The higher bandwidth of the shunt-based sensor leads to the recognisable superimposed step response of the first-order, low-pass filter in the current ${}^{(\alpha,\beta)}\vec{i}_{S,shunt}$. Further results for an operating point at rated torque and standstill are shown in Fig. 9. Due to the shorter active switching states of the converter, the results show a higher impact of distorted current samples due to ringing. Still, the noise of the current samples is reduced for both sensors. Again, the results from the shunt-based sensor show the higher bandwidth of the sensor.

In the next results, the effect on the output voltage ${}^{(\hat{d}\hat{q})}\vec{v}^*$ of the current controller is investigated. In Fig. 10, the spectra of the voltage ${}^{(\hat{d}\hat{q})}\vec{v}^*$ of the current controller are shown for steady-state operation at standstill with no-load. By comparing the amplitudes of the spectra without and with using the the proposed filter, one can see less noise when using the filter. The difference between the two spectra in the frequency range from $f = [1...2]\text{kHz}$ is defined as the damping D.

Results at rated speed and no load are shown in Fig. 11. The results with the Hall-effect-based current sensor show only small differences between using the filter and not using the filter. At standstill, an

(a) Results with a Hall effect-based current sensor

(b) Results with a shunt-based current sensor
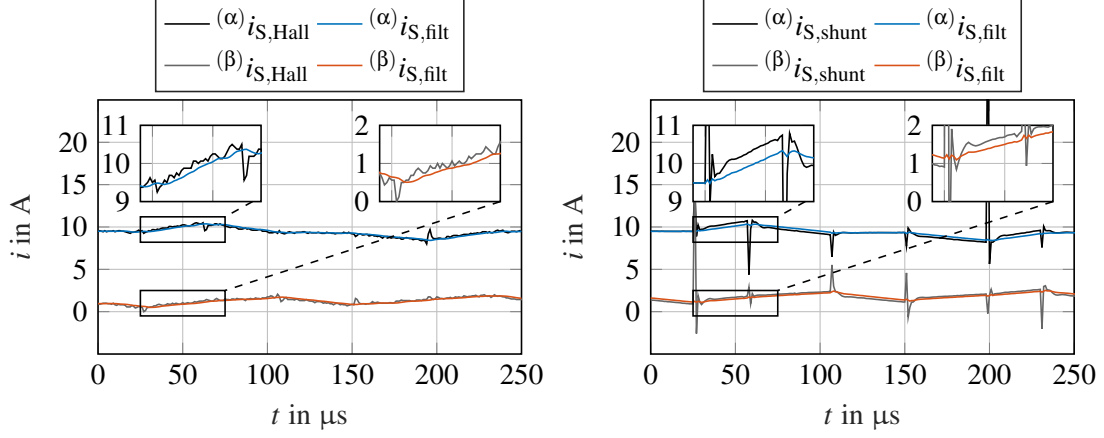
Fig. 8: Experimental results at the operating point of $n = 1000\,^1/_{\min}$ and $M = 2\,\mathrm{Nm}$

(a) Results with a Hall effect-based current sensor

(b) Results with a shunt-based current sensor

Fig. 9: Experimental results at the operating point of $n = 0\,^1/_{\min}$ and $M = 47\,\mathrm{Nm}$

(a) Results with a Hall effect-based current sensor

(b) Results with a shunt-based current sensor
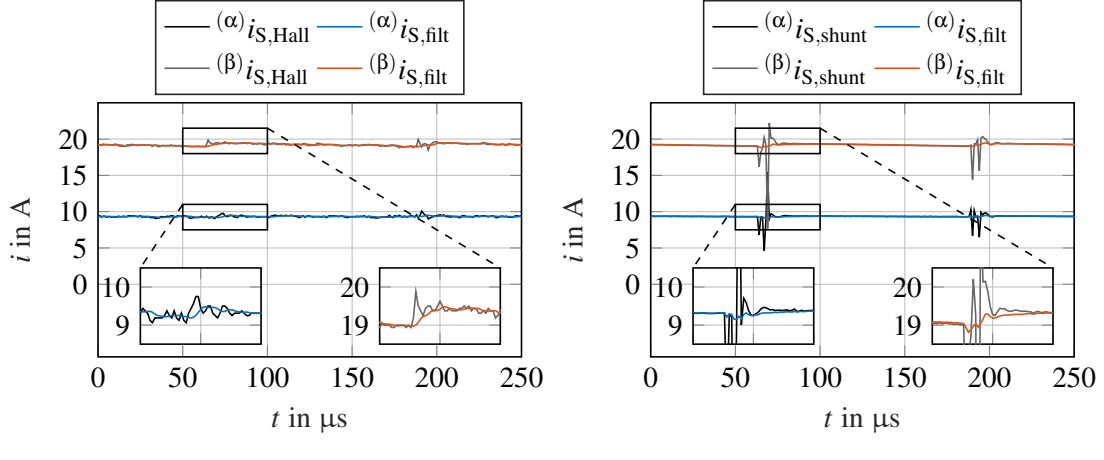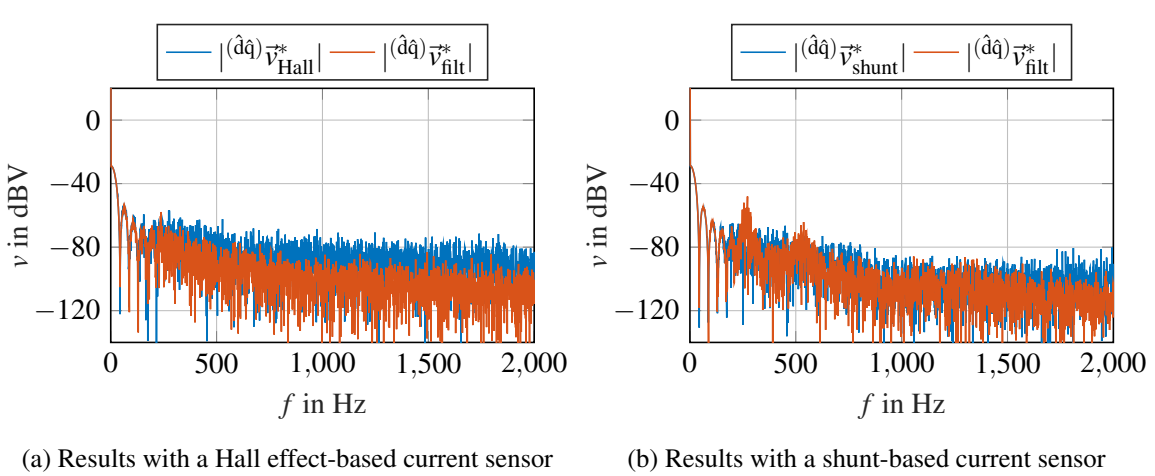
Fig. 10: Experimental results showing the spectra of the voltage $^{(\hat{d}\hat{q})}\vec{v}^*$ at the operating point of $n = 0\,^1/_{\min}$ and $M = 0\,\mathrm{Nm}$

improvement is achieved, because the white noise of the measurement is reduced. Now, at a higher speed, the noise is generated systematically by the experimental setup. Thus, the signal-to-noise ratio is not improved. But for the shunt-based current sensor, an improvement becomes evident. This can be

explained by the high output level of the PWM. Due to this, the effect of ringing leads to a distorted current sample when the filter is not being used.


(a) Results with a Hall-effect-based current sensor

(b) Results with a shunt-based current sensor
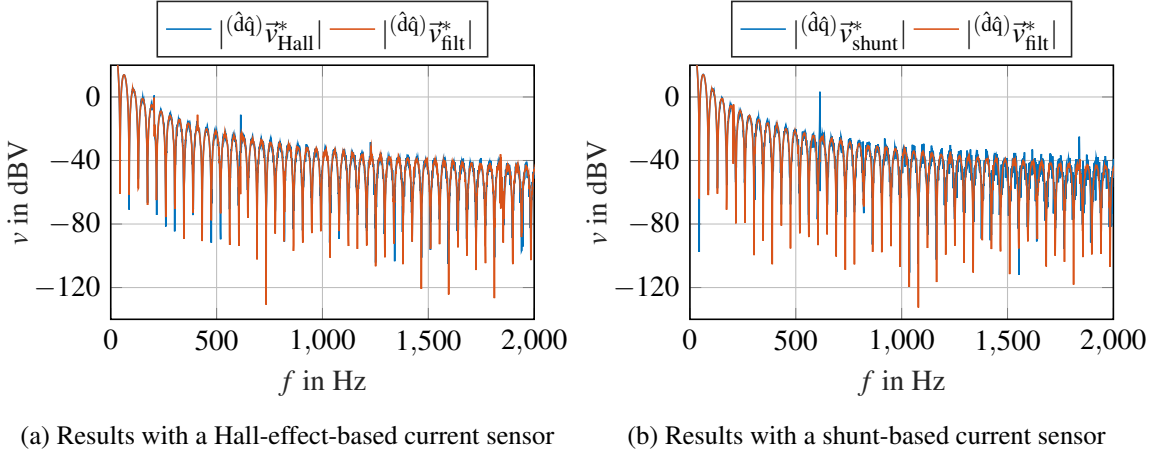
Fig. 11: Experimental results showing the spectra of the voltage $^{(\hat{d}\hat{q})}\vec{v}^*$ at the operating point $n = 1500\,^1/\text{min}$ and $M = 0\,\text{Nm}$

A comparison of the damping of the voltage noise $^{(\hat{d}\hat{q})}\vec{v}^*$ for the whole operating range is shown in Fig. 12. For the results with the Hall-effect- and shunt-based current sensors, a positive effect can be seen at standstill with damping ranging up to 16 dB for the Hall-effect-based sensor and up to 11 dB for the shunt-based sensor. In the area of mid-range speed only, small differences are apparent. For the shunt-based sensor, the reduction of ringing effects at high speed leads to a damping of up to 19 dB, while there is no difference at high speed for the Hall-effect-based sensor.


(a) Results with a Hall-effect-based current sensor

(b) Results with a shunt-based current sensor
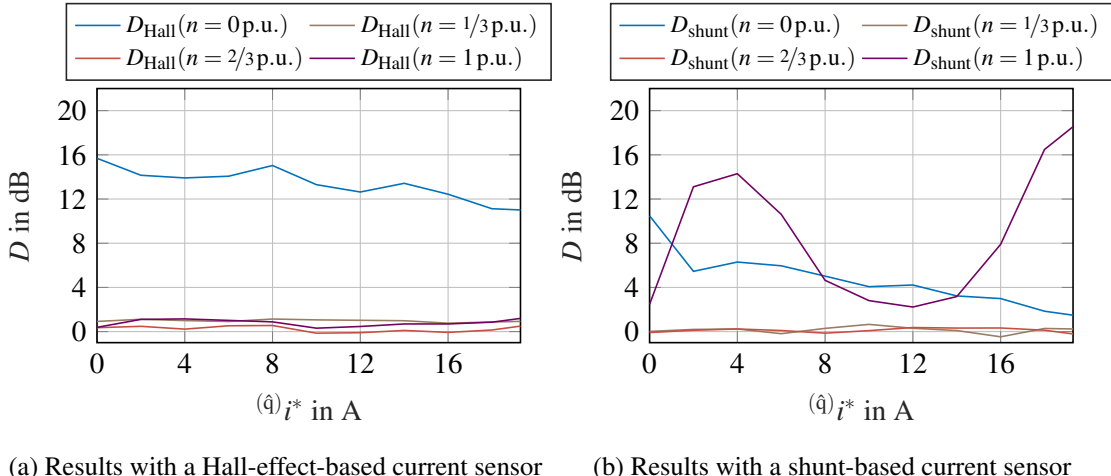
Fig. 12: Experimental results showing damping across the operating range of the machine

Conclusion

The proposed filter for high-bandwidth, high-sampling-rate current measurement meets the requirement of a low phase shift. Through the use of this filter, the signal-to-noise ratio of the investigated current measurements is improved, leading to less noisy current control of the electrical machine investigated. In future work, this filter can be experimentally validated with synchronous machines.

References

[1] S.-H. Song, J.-W. Choi, and S.-K. Sul, "Current measurements in digitally controlled AC drives," *IEEE Industry Applications Magazine*, vol. 6, no. 4, pp. 51–62, Jul. 2000.

[2] F. Briz, D. Díaz-Reigosa, M. W. Degner, P. García, and J. M. Guerrero, "Current sampling and measurement in PWM operated AC drives and power converters," in *The 2010 International Power Electronics Conference*, Jun. 2010, pp. 2753–2760.

[3] A. Mertens and D. Eckardt, "Voltage and current sensing in power electronic converters using sigma-delta A/D conversion," *IEEE Transactions on Industry Applications*, vol. 34, no. 5, pp. 1139–1146, Sep. 1998.

[4] P. Landsmann, D. Paulus, A. Dötlinger, and R. Kennel, "Silent injection for saliency based sensorless control by means of current oversampling," in *2013 IEEE International Conference on Industrial Technology (ICIT)*, Feb. 2013, pp. 398–403.

[5] B. Weber, G. Lindemann, and A. Mertens, "Reduced observer for anisotropy-based position estimation of PM synchronous machines using current oversampling," in *2017 IEEE International Symposium on Sensorless Control for Electrical Drives (SLED)*, Sep. 2017, pp. 121–126.

[6] G. Garcia, J. Santisteban, and S. Brignone, "Iron losses influence on a field-oriented controller," in *Proceedings of IECON'94 - 20th Annual Conference of IEEE Industrial Electronics*, vol. 1, Sep. 1994, pp. 633–638 vol.1.

[7] D. S. Ding, X. J. Wang, and X. P. Luo, "A Study of Vector Control of Induction Machine Considering Iron Loss," *Advanced Materials Research*, vol. 268-270, pp. 129–137, Jul. 2011.

[8] R. D. Lorenz and D. B. Lawson, "Performance of Feedforward Current Regulators for Field-Oriented Induction Machine Controllers," *IEEE Transactions on Industry Applications*, vol. IA-23, no. 4, pp. 597–602, Jul. 1987.

[9] S. Kim, J.-I. Ha, and S.-K. Sul, "PWM Switching Frequency Signal Injection Sensorless Method in IPMSM," *IEEE Transactions on Industry Applications*, vol. 48, no. 5, pp. 1576–1587, Sep. 2012.